Journal of Advanced Ceramics
先进陶瓷
ISSN 2226-4108
CN 10-1154/TQ
清華大学出版社 Tsinghua University Press
SciOpen

J Adv Ceram 2026, **15**: 9221319

https://doi.org/10.26599/JAC.2026.9221319

Research Article

Synergistic enhancement of dielectric properties and reliability of $BaTiO_3$-based MLCC via compositional gradient design and nano-domain engineering

Zhenhao Cai[1,2,†], Saiwei Luan[1,†], Huizhen He[1,3], Wentao Huai[1,3], Zhouyi Xu[1], Zhangping Wu[1], Jun Yang[4], Zhenxiao Fu[5], Xiuhua Cao[5] ,Lei Zhang[1,*],Rong Sun[1]

[1]*Shenzhen Institute of Advanced Electronic Materials, Shenzhen Institutes of Advanced Technology, Chinese Academy of Sciences, Shenzhen 518055, China*

[2]*University of Chinese Academy of Sciences, Beijing 101400, China*

[3]*Southern University of Science and Technology, Shenzhen 518055, China*

[4]*Department of General Education, Army Engineering University of PLA, Nanjing 211101, China*

[5]*State Key Laboratory of Advanced Materials and Electronic Components, Guangdong Fenghua Advanced Technology Holding Co., Ltd, Zhaoqing 526000, China*

† The authors contribute equally.

*Corresponding author.

E-mail addresses: zhanglei@siat.ac.cn

Received: December 9, 2025; Revised: May 11, 2026; Accepted: May 13, 2026

ABSTRACT

Dielectrics with high dielectric constant, low dielectric loss, and good temperature stability are essential for $BaTiO_3$-based MLCCs to meet the escalating demands of 5G communication technologies. However, challenges remain in further optimizing dielectric properties due to the correlation between these parameters. This study proposes a synergistic design strategy that overcomes this limitation through the coupling of compositional gradient control and nano-domain engineering. An optimized 900 ℃ pre-sintering process enables precise structural regulation, forming a tetragonal barium titanate core surrounded by a dopant-enriched graded compositional-gradient shell structure. Atomic-scale analysis confirms that the gradient design achieves directional distribution of Y/Mg/Mn dopants, stabilizes the highly tetragonal core, and confines oxygen vacancy-related defects to the shell region. This defect-localization effect suppresses long-range vacancy migration, thereby significantly enhancing insulation resistance and breakdown strength. Concurrently, the formation of relaxor-like polar nanodomains not only contributes to high dielectric constant but also optimizes the temperature stability of dielectric constant. Ultimately, the prepared ceramic materials exhibit a high dielectric constant (ε_r > 2200), excellent thermal stability meeting X8R standards (−55–150 ℃, $\Delta C/C_{25℃} \leq \pm 15\%$), and enhanced breakdown strength (> 6.7 kV/mm). This finding implies that the synergistic regulation of compositional gradients and nano-domain engineering may be a promising strategy for designing both high capacitance and robust reliability dielectric materials and provides a broad opportunity for the development of other dielectric materials.

Keywords

Compositional gradient design; Nano-domain engineering; $BaTiO_3$-based MLCCs; Breakdown strength; Temperature stability (X8R); Oxygen vacancy confinement

1. Introduction

Multilayer ceramic capacitors (MLCCs) based on barium titanate ($BaTiO_3$, BT) are indispensable components in modern electronic devices [1]. However, they often encounter a trade-off between high dielectric performance (e.g., high dielectric constant and stable capacitance) [2,3] and robust reliability (e.g., resistance to breakdown and aging) [4,5]， particularly under extreme conditions such as elevated temperatures and high electric fields [6–8]. Achieving both simultaneously remains a formidable challenge.

Despite their wide application, BT-based MLCCs suffer from intrinsic material limitations [9,10]. A major drawback is the sharp dielectric anomaly near the Curie temperature (~120 ℃), where a pronounced dielectric constant peak severely destabilizes capacitance over broad operating ranges [11–13]. This temperature-dependent dielectric response makes it difficult to satisfy reliability standards such as X7R or X8R in practical devices [14–16]. Furthermore, the relatively low dielectric breakdown strength of conventional BT ceramics restricts energy storage density and exacerbates degradation under high electric fields [17–19]. These coupled drawbacks—thermal instability near the Curie point and limited breakdown resistance-constitute the central bottlenecks for advancing BT-based MLCCs [20–22].

To enhance dielectric performance, several strategies have been explored, including elemental doping, core–shell architecture optimization, and defect dipole engineering. For instance, Zhu et al. [23] employed Dy-Mg co-doping to optimize core–shell structures, achieving $\varepsilon_r \approx 2000$ and improved DC bias stability. Nevertheless, this approach requires precise control of dopant distribution and sintering conditions, which complicates large-scale processing and risks compositional inhomogeneity. Zhang et al. [24] suggested the use of Mn-induced defect dipoles to improve dielectric properties and reliability; however, the effectiveness of defect dipoles is highly dependent on dopant chemistry and processing atmosphere, limiting general applicability. Ma et al. [25] incorporated $La(Mg_{1/2}Zr_{1/2})O_3$ to induce polar nano-regions (PNRs) and relaxor-like behavior, enhancing energy storage density. However, this method often sacrifices

room-temperature dielectric constant and poses challenges in maintaining microstructural consistency.

On the reliability side, efforts have focused on boosting breakdown strength and suppressing insulation resistance degradation through advanced defect control, reoxidation treatments, and microstructure refinement [26]. Huang et al. [27] showed that high-pressure reoxidation significantly reduces oxygen vacancy concentration at the BT/Ni electrode interface, increasing the Schottky barrier and breakdown strength. However, this method introduces additional cost, complexity, and processing time, and may even induce stresses or cracks in ultra-thin dielectric layers. Lv et al. [28] suggested that Mg substitution in $BaTi_{1-x}Mg_xO_3$ effectively suppresses grain growth and pins oxygen vacancy migration, improving reliability. The limitation, however, is an extremely narrow compositional window; slight deviations rapidly degrade dielectric performance, complicating reproducibility in large-scale manufacturing. Izawa et al. [29] further emphasized the importance of uniform fine-grained microstructures with well-controlled core–shell configurations to suppress degradation propagation. However, achieving such homogeneity throughout the large volume of commercial MLCCs remains highly challenging, particularly as dielectric layers continue to thin.

In summary, while these strategies provide valuable insights, most either improve only one aspect of the performance-reliability balance or introduce significant processing complexities [30]. In this work, a synergistic strategy is proposed that integrates compositional gradient design with nanodomain engineering within a single, streamlined sintering process. This approach yields a unique graded compositional-gradient shell structure, consisting of a tetragonal BT core and a dopant-enriched cubic shell. Such architecture simultaneously enhances tetragonality, redistributes dopants, and confines oxygen vacancies. The resulting ceramics exhibit superior dielectric properties (ε_r > 2200, which complies with the EIA X8R standard), high breakdown strength (> 6.7 kV/mm), and excellent reliability, evidenced by increased activation energy and suppressed oxygen vacancy migration. Moreover, the concurrent formation of nanoscale polar domains induces relaxor-like behavior, boosting dielectric constant

without the conventional trade-offs. This integrated strategy thus overcomes the limitations of prior approaches, offering a more robust, scalable, and manufacturable pathway toward next-generation high-performance MLCCs.

2. Experimental

2.1. Sample fabrication

In this study, a solid-state reaction method was employed to fabricate $BaTiO_3$ (BT)-based ceramics with varying dopant configurations. Detailed raw material specifications are provided in Table S1. Two distinct processing schemes were investigated: a conventional one-step sintering process and a modified two-step sintering process incorporating a pre-sintering stage. For the one-step sintering (Un-Pre), BT powder was directly mixed with Y_2O_3, MgO, SiO_2, and MnO_2 in a single stage. Conversely, the two-step sintering involved an initial pre-treatment of $BaTiO_3$ and Y_2O_3 (pre-sintering) followed by a second blending stage with MgO, SiO_2, and MnO_2 to form the final composition, as illustrated in the process flow (Fig. S1).

This sequential introduction of dopants was strategically designed to leverage their disparate diffusion kinetics. Specifically, Y_2O_3 was introduced during the pre-sintering stage to establish a stable diffusion-modulating gradient, which effectively preserves the ferroelectric core. MgO, MnO_2, and SiO_2 were subsequently added to confine their functional roles-such as grain-growth regulation, relaxor-like modification, and reduction resistance-primarily within the shell region. Samples without pre-sintering are designated as Un-Pre, while those pre-sintered at 800 ℃, 900 ℃, and 1000 ℃ are labeled as Pre-800, Pre-900, and Pre-1000, respectively. Sintering conditions and stoichiometric dopant concentrations are summarized in Table S2.

Stoichiometric amounts of raw powders were homogenized via planetary ball milling in ethanol with zirconia media (2 mm diameter) at a mass ratio of 1:1:1.5 (BT-based powder: ethanol: zirconia balls) at 480 rpm for 24 hours. The resulting slurry was dried at 90 ℃ for 24 hours and then granulated with an 8 wt% polyvinyl alcohol (PVA) binder solution. After sieving through a 200-mesh screen, the granules were uniaxially

pressed into green pellets 8 mm in diameter, approximately 1.2 mm in thickness, under a pressure of 356 MPa. Sintering was conducted in a controlled-atmosphere tube furnace under the following precisely defined thermal schedule: samples were initially heated from ambient temperature to 300 ℃ at 2 ℃/min with a 30 min hold to ensure moisture removal. Subsequently, the temperature was raised to 600 ℃ at 2 ℃/min for another 30 min hold to volatilize organic residues. Thereafter, the samples were heated to the peak sintering temperature of 1250 ℃ at 4 ℃/min and held for 120 min under a flowing reducing atmosphere (1.5 vol% H_2/98.5 vol% N_2, $pO_2 \approx 10^{-13}$ atm) to achieve full densification. Finally, the furnace was cooled to room temperature at a controlled rate of 10 ℃/min. Prior to electrical testing, ceramic samples were polished on both sides, coated with high-temperature silver paste, and fired in air at 600 ℃ for 30 min to form robust electrode interfaces.

2.2. Characterization

The phase composition and lattice parameters of the ceramics were characterized by X-ray diffraction (XRD, D8 Advance, Bruker, Germany) using Cu Kα radiation (λ = 1.5406 Å), and the tetragonality (c/a) was calculated through Rietveld refinements with the FullProf suite. Raman spectroscopy (LabRAM HR, HORIBA, Japan) with 532 nm excitation in the range of 100–1100 cm^{-1} was used to identify tetragonal/cubic phases, local lattice distortion and oxygen-vacancy-related features. The grain morphology was examined by field-emission scanning electron microscopy (FE-SEM, NOVA NANOSEM 450, FEI, USA) in both SE and BSE modes, and grain sizes were statistically analyzed with Nano Measurer software. Elemental distributions were further confirmed by energy-dispersive spectroscopy (EDS). For atomic-scale characterization, thin lamellae were prepared by focused ion beam (FIB, Helios 5 UX, Thermo Scientific, USA) and analyzed by high-resolution transmission electron microscopy (HRTEM, JEM-2100F, JEOL, Japan). Selected-area diffraction patterns (SADPs), lattice fringes, and interfacial defects were obtained, while scanning transmission electron microscopy (STEM-HAADF, Spectra 300, ThermoFisher, USA)

combined with EDS and electron energy-loss spectroscopy (EELS) was used to investigate oxygen-vacancy distributions. Electron paramagnetic resonance (EPR, EMXplus-6/1, Bruker, Germany) spectra were recorded at the X-band (~9.5 GHz) at room temperature. X-ray photoelectron spectroscopy (XPS, EscaLab 250Xi, Thermo Scientific, USA) was additionally employed to analyze surface composition and chemical states.

Dielectric properties were measured using a broadband dielectric spectrometer (Alpha-A, Novocontrol GmbH, Germany) coupled to an LCR meter (4980A, Keysight, USA) in the temperature range of −60–200 ℃. Temperature- and frequency-dependent dielectric constant (ε_r) and dielectric loss (tan δ) were recorded, and Vogel-Fulcher fitting was applied to analyze relaxor behavior. Polarization–electric field (*P*-*E*) hysteresis loops were obtained using a ferroelectric tester (Radiant Precision Multi-Ferric II, USA) at 10^3 Hz under silicone oil. The dielectric breakdown strength (BDS) was evaluated with a programmable withstand voltage tester (CS9912BX, Changsheng, China) at a constant ramp rate of 2 V/s. Electrochemical impedance spectroscopy (EIS, Balab DMS1000) was performed at 400–600 ℃ over 10^1–10^6 Hz. The highly accelerated life test (HALT) was performed at 250 ℃ under an electric field of 1.5 kV/mm for 48 h, using a high resistance meter (6517A, Keithley, USA) with a plane heater. Thermally stimulated depolarization current (TSDC) was measured using a Keithley 6517B after polarization at 1–5 kV/cm, cooling to −50 ℃, and subsequent heating at 4 ℃/min.

3. Results and discussion

3.1. Microstructure and phase

As illustrated in the lattice schematic of Fig. 1(a), the ceramic grains exhibit a distinct core–shell configuration, where the inner core retains a tetragonal structure while the outer shell adopts a cubic symmetry [31]. Although the shell region exhibits a cubic symmetry compared to the tetragonal core, both regions belong to the same

$BaTiO_3$-based lattice, reflecting a structural modulation within a single phase rather than the coexistence of distinct shells or secondary phases. Fig. 1(c) shows that the diffraction peaks of the doped ceramics exhibit a clear rightward shift without the emergence of secondary phases, indicating lattice contraction. In the present doping system, Mg^{2+} and Mn^{2+} preferentially occupy B-sites (substituting Ti^{4+}), whereas the rightward XRD peak shift suggests that Y^{3+} (with a smaller ionic radius than Ba^{2+}) occupies A-sites. As evidenced by the XRD peak-shift behavior in the preliminary experiments shown in Fig. S2, where the Y_2O_3 content varies from 0.1 to 1.0 mol%, the diffraction peaks initially shift toward higher 2θ angles and subsequently shift back toward lower angles with increasing Y content. This non-monotonic peak evolution indicates that Y^{3+} preferentially substitutes at the A-sites at low doping levels, followed by progressive B-site incorporation at higher concentrations. At a Y_2O_3 content of ~0.3 mol%, the trend suggests that A-site incorporation becomes dominant and approaches saturation, beyond which additional Y increasingly occupies B-sites.

Fig. 1(d–e) present the Rietveld refinement results, from which lattice constants and tetragonality (*c/a*) were extracted. Multiphasic refinement further quantified the phase ratio between the cubic shell and tetragonal core of BT grains [32]. Quantitative Rietveld refinement (Fig. 1(d–e)) indicates that Pre-900 sample exhibits a slightly higher tetragonality (*c/a* = 1.0077) than Un-Pre sample (*c/a* = 1.0065), accompanied by moderate grain coarsening (average size (226.5 ± 18.4) nm *vs* (195.1 ± 21.3) nm, see Fig. 3(a–b)). Since the increase in grain size from the Un-pre to the Pre-900 sample is non-negligible, its contribution to the enhancement of tetragonality cannot be completely excluded. However, the *c/a* ratio does not scale linearly with grain size in this fine-grained regime [33], suggesting that grain coarsening alone is insufficient to fully explain the observed increase in tetragonality. Although grain-size effects may contribute to this trend, the relatively small variation in grain size suggests that compositional redistribution and defect modulation play a more dominant role. Instead, the increase in *c/a* is more reasonably associated with dopant redistribution induced by pre-sintering, which leads to the formation of a graded compositional core-shell structure. This gradual compositional variation introduces distributed lattice distortion,

which can act as a strain-buffering region by alleviating localized stress accumulation near the core-shell transition. As a result, the tetragonal core is able to better maintain its intrinsic lattice distortion. The higher dielectric constant (ε_r) observed in Pre-900 sample thus originates from a more ordered tetragonal core and not from abnormal grain growth. As illustrated in Fig. 2, this results in a well-defined graded compositional-gradient shell structure. Here, the term "graded compositional-gradient shell" refers to a single shell region with a continuous dopant gradient rather than two distinct shells or phases. In this region, Y is preferentially enriched toward the inner side of the shell, while Mg/Mn exhibit higher concentrations toward the outer shell and gradually increase toward the grain boundary. For descriptive convenience, this graded shell is further segmented into Shell I and Shell II based on EDS line-scan profiles, where the boundary is operationally defined by the positions at which the local concentrations of Y and Mg/Mn decrease to approximately ~1 at.%. No sharp microstructural boundary or contrast change is observed in TEM, indicating that this segmentation reflects a purely chemical gradient rather than a physical interface. Additional XRD patterns of samples pre-sintered at different temperatures (Fig. 1(c)) reveal that increasing the pre-sintering temperature sharpens the (002)/(200) peak splitting near 45°, suggesting a clearer core–shell separation. This behavior suggests that moderate pre-sintering promotes dopant redistribution and clearer core–shell separation. However, At higher pre-sintering temperatures (e.g., 1000 ℃), BT enters an active nucleation regime in which Y tends to locally enrich, leading to premature secondary-phase precipitation during subsequent sintering[34]. Therefore, 900 ℃ emerges as the optimal pre-sintering temperature. Furthermore, the quantitative phase analysis in Fig. 1(f) reveals that increasing the pre-sintering temperature leads to an expansion of the cubic shell fraction and a corresponding decrease in the overall tetragonal phase ratio. However, this structural evolution facilitates the expulsion of dopant ions from the grain interior, resulting in a purified core with reduced dopant concentration and, consequently, enhanced tetragonality despite the reduced core volume.

Raman spectra excited with a 532 nm laser (Fig. 1(b)) further confirm these structural features. The peaks are consistent with those of pure BT, where the 522 cm^{-1}

peak corresponds to the cubic phase ($A_1(TO_2)$ mode) and the 305 cm^{-1} peak corresponds to the tetragonal phase (B_1 mode). The broadening of the B_1 mode in Pre-900 sample suggests enhanced local structural disorder and strain gradient within the lattice, which is consistent with the presence of nanoscale polar regions and compositional heterogeneity revealed by STEM [35,36].

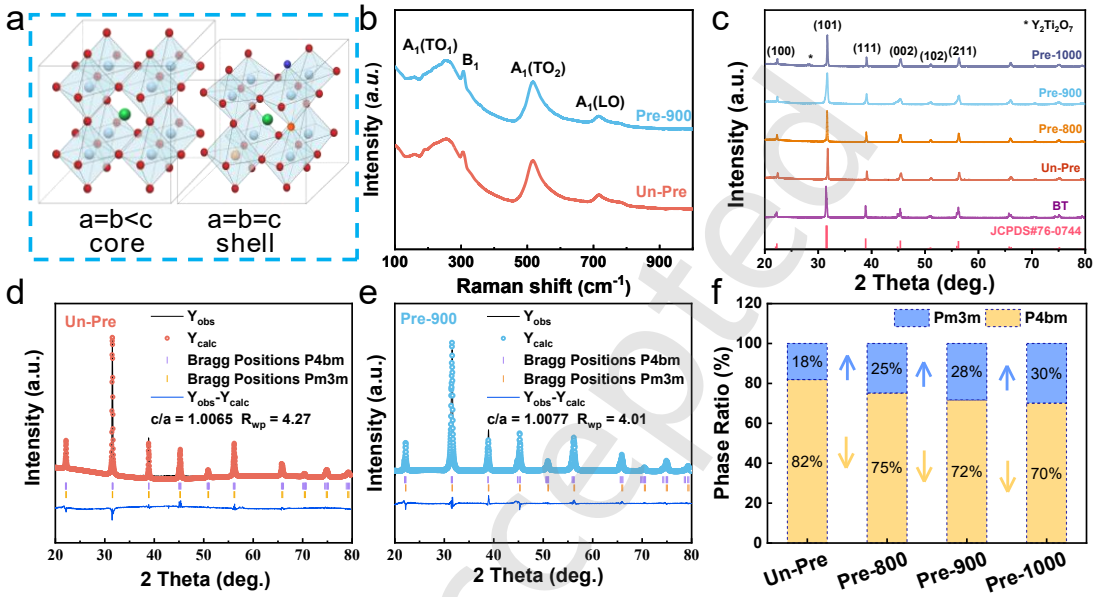

Fig. 1 (a) The lattice structure of core-shell. (b) Raman spectra under 532 nm excitation. (c) XRD patterns of BT ceramics. (d–e) Rietveld refinement profiles of Un-Pre and Pre-900 samples. (f) Cubic–tetragonal phase fractions.

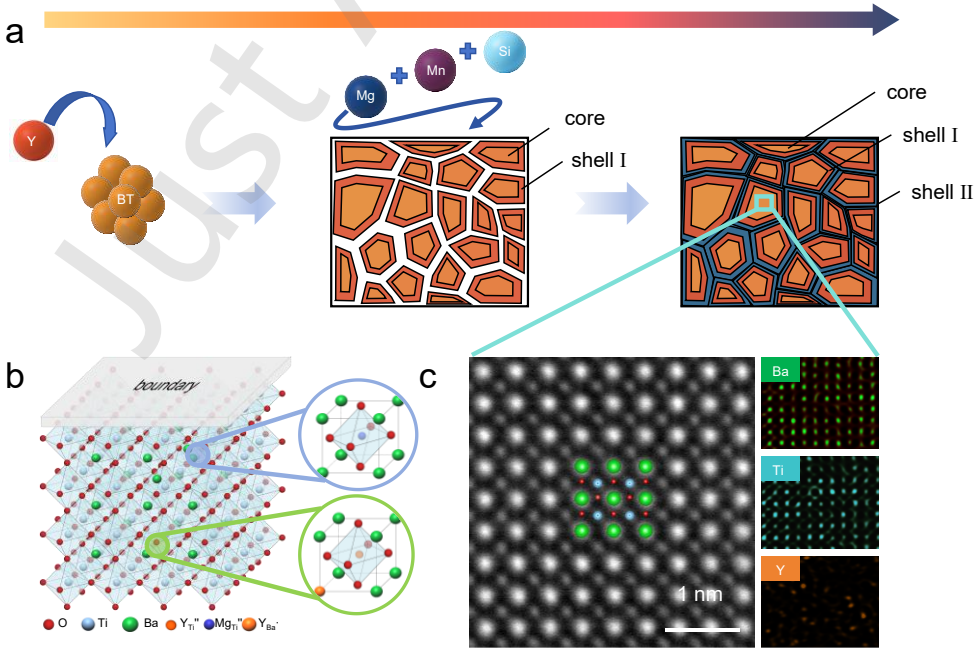

Fig. 2 Proposed structural model of the compositional-gradient grain for the Pre-900 ceramic, representing the spatial distribution of the tetragonal core and dopant-modified shell regions inferred from structural and elemental characterizations.

The microstructural features of the Pre-900 and Un-Pre samples were further investigated by FE-SEM and HRTEM, as shown in Fig. 3. Statistical analysis of SEM images (Fig. 3(a–b)) yields average grain sizes of 226.54 nm for Pre-900 sample and 195.12 nm for Un-Pre sample. After pre-sintering, the fraction of smaller grains decreases, and the overall grain morphology becomes more uniform and rounded. It should be noted that the improved grain-size uniformity observed in the Pre-900 sample does not indicate an overall enhancement of grain-growth kinetics. Instead, the more continuous and homogeneous shell coverage induced by pre-sintering homogenizes grain-boundary chemistry and mobility, suppressing local fluctuations in boundary migration. As a result, the retention of abnormally small grains is reduced and a narrower grain-size distribution is obtained, despite the intrinsic grain-growth–inhibiting effect of shell-forming dopants. TEM images and EDS line scans (Fig. 3(c–d)) occasionally reveal isolated submicron contrast features on BT grain surfaces, likely associated with the decomposition of residual hydroxyl and carbonate species in the hydrothermally synthesized powders during sintering. Despite this, the ceramics are highly densified, with relative densities of 95.4% (Un-Pre) and 96.1% (Pre-900). EDS line profiles (Fig. 3(e–f)、Fig. S5) indicate that Mg and Y are both concentrated in the shell regions. For the Pre-900 sample, their concentration profiles exhibit two distinct gradient regions, here denoted Shell I and Shell II. In contrast, the Un-Pre sample shows only a single shell with overlapping dopant peaks. The line profile shown in Fig. 3(e–f) is a representative example selected to illustrate this characteristic gradient distribution.

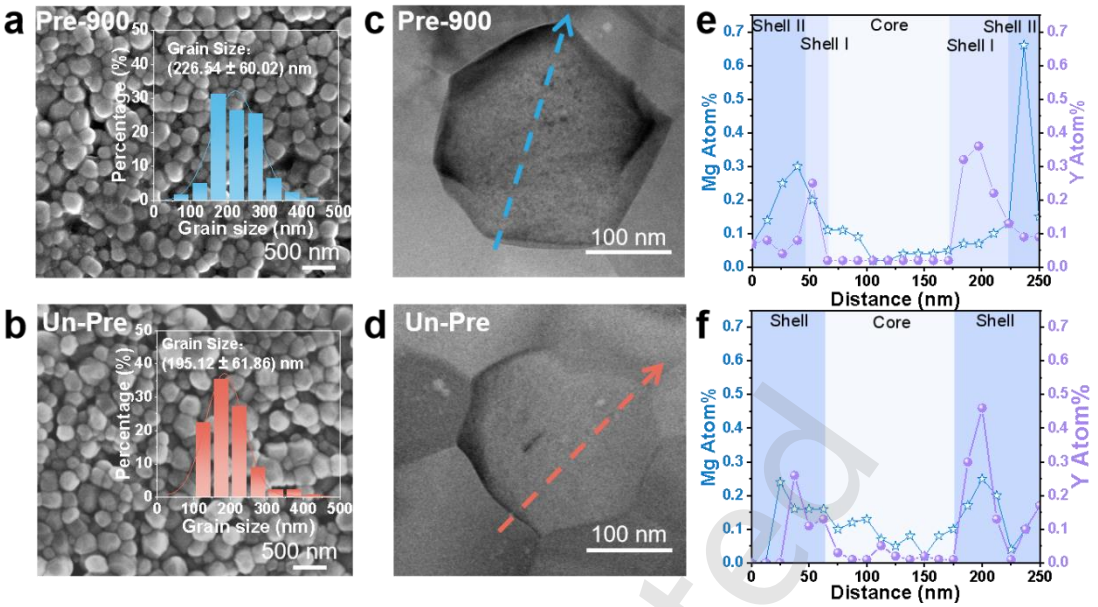

Fig. 3 (a–b) SEM images with grain size statistics. (c–d) TEM morphology of individual grains. (e–f) EDS line scans showing dopant distribution across shells.

To further highlight the internal grain modifications induced by pre-sintering, STEM-HAADF imaging was conducted (Fig. 4–5). The HAADF images resolve the periodic arrangement of Ba and Ti atomic columns at the grain edges. As shown in Fig. 4, doping alters the intensity contrast of the A-site (Ba) and B-site (Ti) atomic columns, reflecting compositional variations. The intensity mapping indicates that, in the Pre-900 sample, regions with relatively higher A-site and B-site atomic-column intensities are located closer to the grain interior than in the Un-Pre sample, and the corresponding A/B-site intensity ratio is also higher. This observation suggests a more inwardly shifted and compact core region after pre-sintering. It should be noted that the intensity contrast is interpreted in a qualitative manner, since atomic-column intensity in STEM is governed primarily by the average atomic number (Z-contrast) of the constituent elements rather than their absolute concentration. In this context, Mg and Mn, owing to their relatively low atomic numbers, contribute weakly to the overall column intensity and are therefore difficult to resolve unambiguously under the present imaging conditions. Consequently, the STEM intensity mapping mainly reflects the redistribution of heavier A- and B-site species, while the segregation behavior of Mg/Mn is more reliably captured by complementary EDS line scans and EELS analyses. When considered together with the EDS results, these observations suggest that Y^{3+} is

preferentially enriched in the inner region during pre-sintering, consistent with predominant A-site incorporation, thereby forming a defect-rich isolation layer that hinders the inward diffusion of subsequently introduced dopants (e.g., Mg^{2+}, Mn^{2+}). Fig. 2(b) schematically illustrates a conceptual model for dopant redistribution and defect organization inferred from the combined experimental observations, later-introduced elements such as Mg and Mn tend to accumulate in the outer shell (Shell II) during high-temperature growth. This defect-segregated structure is beneficial for suppressing oxygen vacancy migration and thereby enhances MLCC reliability.

The displacement of B-site cations was further examined, as shown in Fig. 5. In BT, B-site cation displacement within TiO_6 octahedra is intrinsic: Ti^{4+} ions shift along the c-axis to generate spontaneous polarization [37]. In pure BT, these displacements are aligned, producing long-range ferroelectric order. Upon doping, lattice distortions from ionic size mismatch alter the polarization directions, breaking long-range order and forming nanoscale polar domains that enhance dielectric response. As shown in Fig. 5(i), the Pre-900 sample exhibits finer and more dispersed nanodomains, whereas the Un-Pre sample retains larger, uniformly oriented domains. Thus, pre-sintering disrupts long-range order and strengthens polarization flexibility. The color-mapped displacement modulus of B-site atoms (Fig. 5(a–b)) further reveals that Pre-900 sample exhibits stronger local displacements within Shell II due to concentrated dopants and defects. This domain configuration contributes to enhanced dielectric response, as polarization gradients at domain walls introduce additional dielectric polarization.

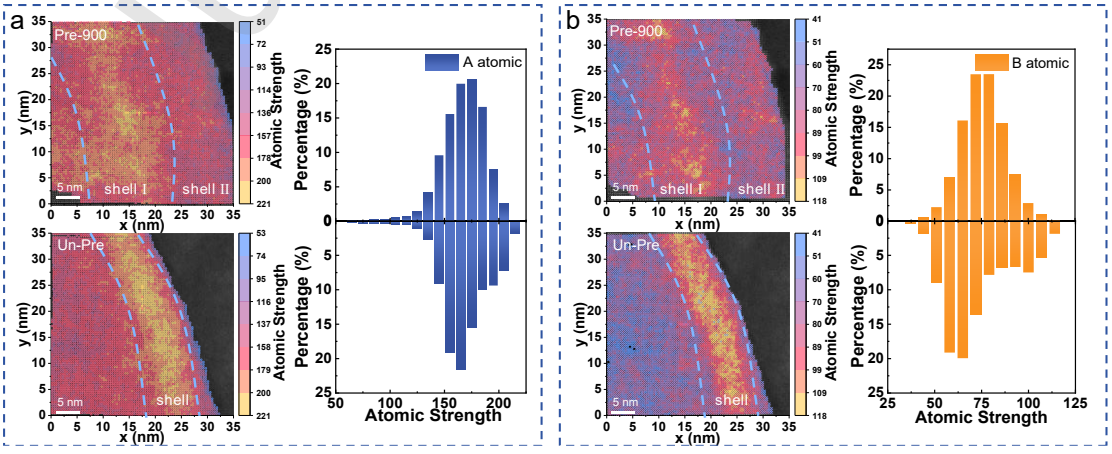

Fig. 4 (a) A-site intensity contrast variations, and statistical intensity profiles of atomic columns at grain boundaries. (b) B-site intensity contrast variations, and statistical intensity profiles of atomic

columns at grain boundaries.

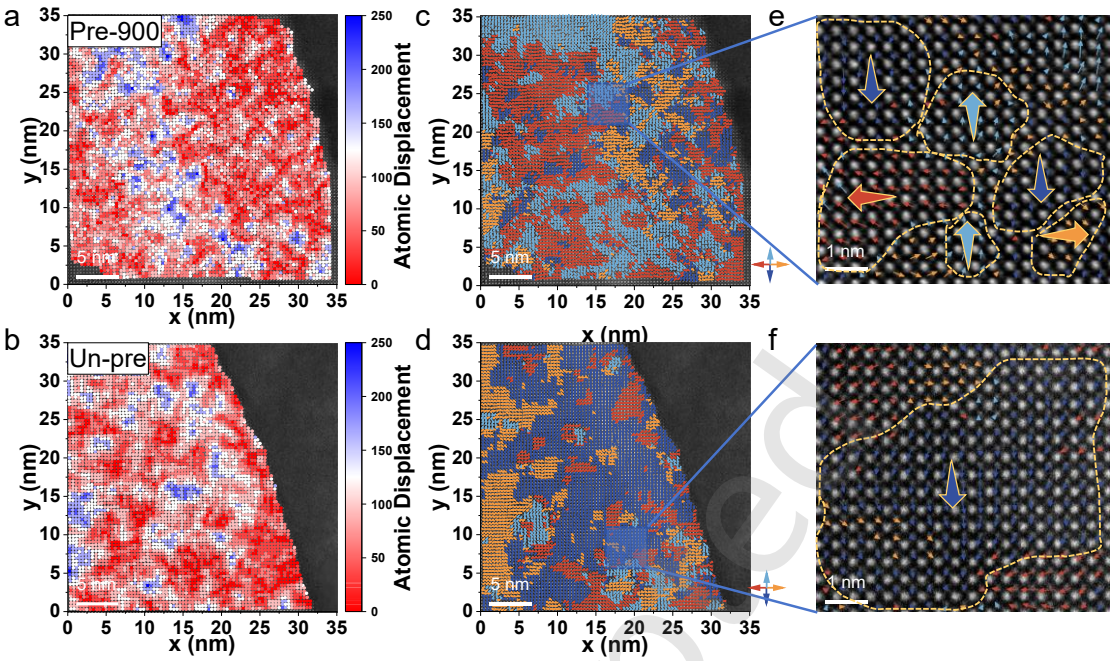

Fig. 5 (a–b) Color-mapped displacement modulus distributions highlighting enhanced local polarization. (c–d) Atomic displacement maps of Pre-900 and Un-Pre samples. (e–f) Local area display of nano-domains.

Fig. 2 and Fig. S4 provide atomic-scale insights into the lattice configuration and compositional distribution of the BT-based ceramics. High-resolution transmission electron microscopy (HRTEM) images reveal a highly coherent and continuous atomic arrangement, indicating that the dopant-modified shell maintains an epitaxial-like relationship with the BT core, with no observable secondary phases or incoherent interfaces. Due to the subtle nature of the tetragonal-to-cubic lattice distortion, the lattice fringes exhibit high visual uniformity; consequently, the characteristic core–shell hierarchy is primarily resolved through chemical heterogeneity rather than geometric structural distinctions. STEM-EDS elemental mappings (Fig. 2) further confirm that, following the pre-sintering process, dopants are preferentially enriched in the shell region, establishing a distinct compositional gradient. This redistribution, driven by the interplay between controlled diffusion and strain-field interactions during pre-sintering, effectively stabilizes the dielectric response. The synergy between a continuous lattice framework and a chemical gradient provides a robust structural foundation for the observed relaxor-like behavior and enhanced insulation reliability.

3.2. Dielectric property

As the core dielectric material for MLCCs, the dielectric constant of BT ceramics is a crucial performance parameter. To investigate the effect of the pre-sintering process on dielectric behavior, four groups of samples (Un-Pre, Pre-800, Pre-900, and Pre-1000 samples) were measured. The dielectric constant and dielectric loss as functions of temperature from −60–200 ℃ are shown in Fig. 6(a), while Fig. 6(b) shows the temperature coefficient of capacitance. It can be observed that the dielectric constant increases after pre-sintering, particularly for Pre-900 and Pre-1000 samples, which display a pronounced Curie peak near 125 ℃. These samples satisfy the X8R standard ($\Delta C/C_{25℃} \leq \pm 15\%$, −55–150 ℃). With increasing pre-sintering temperature, the room-temperature dielectric constant rises. The Pre-800 sample shows nearly the same value as Un-Pre sample, as the relatively low temperature is insufficient to induce effective BT nucleation and Y incorporation, thereby failing to form a compositional gradient [36]. At 900 ℃, nucleation is promoted, and Y substitution occurs preferentially in the inner region, forming Shell II, which isolates other dopants and enhances the tetragonal phase transition of the core, leading to an elevated Curie peak. When the pre-sintering temperature is further increased, deeper diffusion of Y occurs, suppressing the Curie peak. Thus, Pre-900 sample exhibits the most pronounced difference compared to Un-Pre sample, indicating that 900 ℃ is the optimal pre-sintering condition.

Fig. 6(d–e) compare the dielectric spectra of Un-Pre sample and Pre-900 sample at different frequencies. For Un-Pre sample, the dielectric response is relatively stable across frequency, showing minimal dispersion. In contrast, the Pre-900 sample exhibits noticeable frequency dispersion in its dielectric response. Specifically, as the measurement frequency increases from low (10^1 Hz) to high (10^6 Hz), the maximum dielectric constant gradually decreases, while the temperature of the dielectric peak (T_m) remains nearly unchanged. This behavior suggests a diffuse phase transition with relaxor-like characteristics, rather than a classical relaxor ferroelectric state where T_m typically shifts with frequency. The observed frequency dispersion can be associated with the dynamic response of nanoscale polarization regions. At lower frequencies,

polarization fluctuations and domain-wall motion can follow the external electric field more effectively, resulting in a higher dielectric constant. As the frequency increases, the response of these polarization regions becomes progressively restricted, leading to a reduction in the dielectric constant.

Ferroelectric properties were also analyzed in detail. Using the modified Curie-Weiss law, the degree of phase transition diffuseness was quantified [11]:

$$\frac{1}{\varepsilon}-\frac{1}{\varepsilon_{\mathrm{m}}}=\frac{\left(T-T_{\mathrm{m}}\right)^{\gamma}}{C} \tag{1}$$

where is ε the dielectric constant, ε_m the maximum dielectric constant at Curie temperature T_m, C the Curie constant, and γ the diffuseness index (1 for normal ferroelectrics, 2 for relaxors). The calculated results (Fig. 6(f)) indicate that Pre-900 sample exhibits the largest γ, confirming its strongest diffuse phase transition and the highest fraction of non-tetragonal components, consistent with the compositional gradient analysis above [38].

The electric-field dependence of dielectric constant and polarization-electric field (*P-E*) hysteresis loops were also investigated. As shown in Fig. 6(g), under low AC electric fields, the dielectric constant remains stable due to reversible domain-wall motion, where polarization scales linearly with field. At higher fields, irreversible domain-wall motion is activated, leading to a sharp variation in dielectric constant and nonlinear *P-E* loops [21]. Comparing the Pre-900 and Un-Pre samples, the former shows a more pronounced field dependence, consistent with the nanodomain refinement observed in Fig. 5. This behavior indicates enhanced diffuse polarization characteristics with relaxor-like features, where nanoscale polarization regions can more readily respond to external electric fields, resulting in an increased dielectric constant.

High-field dielectric measurements (Fig. 6(h)) further confirm this: as the applied AC field increases stepwise, the dielectric constant of Pre-900 sample rises rapidly, with the peak corresponding to maximum domain reorientation. This nonlinearity is much stronger than in Un-Pre sample, evidencing more dynamic domain evolution [39,40]. The *P-E* loops measured under an electric field of 4 V/μm are compared in Fig. 6(i).

Pre-900 sample exhibits slimmer loops with a reduced coercive field (E_a), attributed to the presence of nanoscale polar domains that facilitate easier polarization switching.

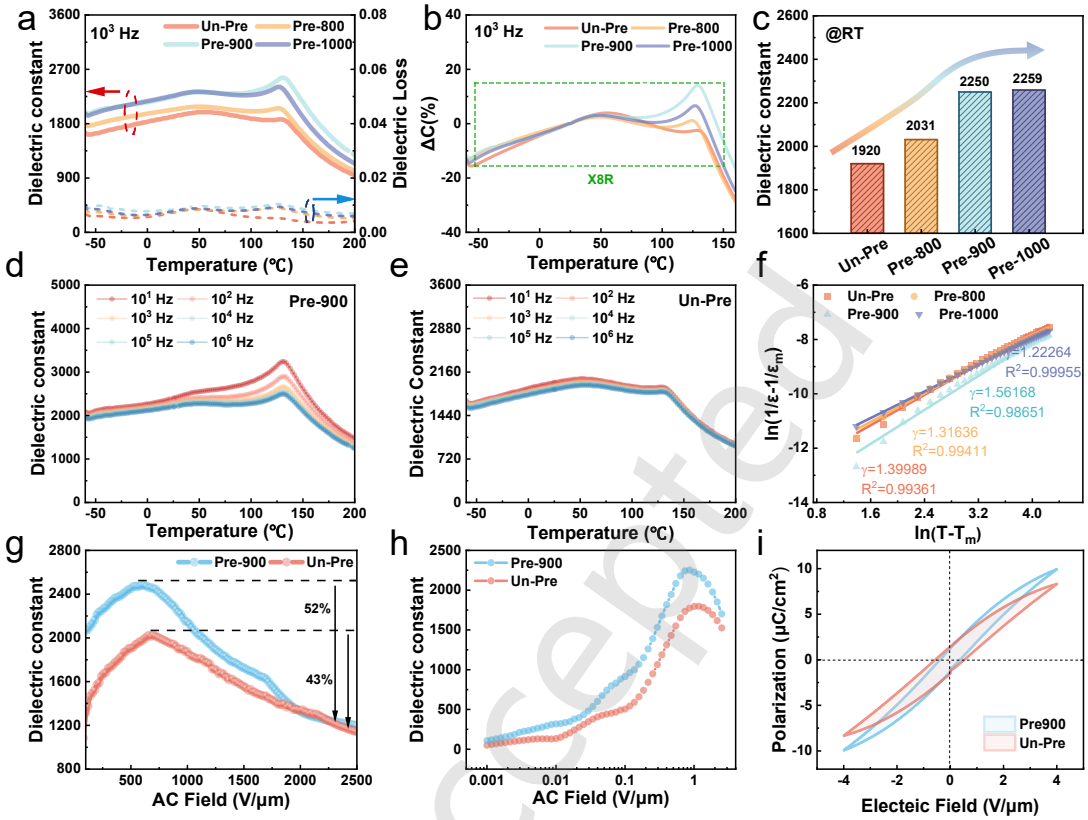

Fig. 6 (a) Temperature-dependent dielectric constant and the dielectric loss of ceramic samples. (b) Capacitance variation with temperature. (c) Dielectric constants comparison at room temperature. (d–e) The change of dielectric constant with different frequencies. (f) Diffuseness index γ from Curie-Weiss fitting. (g) Dielectric constant under AC bias. (h) High-field dielectric response. (i) P-E loops at 4 V/μm.

3.3. Reliability

To evaluate high-temperature electrical reliability, impedance spectroscopy was performed between 400 and 600 ℃. The Cole-Cole plots of real and imaginary impedance versus frequency (Fig. 7(a–b)) display semicircular arcs whose radii gradually shrink with increasing temperature, indicating thermally activated charge transport and a decrease in resistance. Importantly, the Pre-900 sample consistently exhibits higher resistance than Un-Pre sample, confirming that pre-sintering improves insulation. Equivalent circuit fitting was carried out using a 2RC model representing the grain and grain boundary (Fig. S6). The resistance of each component follows the

Arrhenius relation [41]:

$$\ln R = \ln R_0 + \frac{E_a}{k_B T} \tag{2}$$

where R_0 is a constant, E_a is the activation energy for conduction, k_B is Boltzmann's constant, and T is the absolute temperature. As summarized in Fig. 7(c–d), compared to the Un-Pre sample, the Pre-900 sample shows significantly higher activation energies for both grains and grain boundaries. This is attributed to the compositional gradient induced by the pre-sintering process, which generates a much larger potential barrier. This enhanced potential barrier strongly suppresses the long-range migration of oxygen vacancies, as the vacancies are hindered by the increased energy barriers at both grain interiors and grain boundaries and tend to form defect complexes with dopants. Detailed values of the resistances and capacitances of grains and grain boundaries, fitted at different temperatures, are provided in Tables S3 and S4 for further reference.

Dielectric breakdown strength was further evaluated using Weibull statistical analysis on two sets of eight samples. The probability distribution function is expressed as [42,43]:

$$P(E) = 1 - \exp\left[-\left(\frac{E}{\alpha}\right)^{\beta}\right] \tag{3}$$

where E is the applied field, α is the characteristic breakdown field (at 63.2% failure probability), and β is the shape parameter describing data dispersion. As shown in Fig. 7(g), Pre-900 sample achieves an average breakdown strength of 6.707 kV/mm, significantly higher than Un-Pre sample (5.198 kV/mm). This enhancement is attributed to dopant enrichment in the shell and is consistent with the higher shell activation energy discussed above [44]. Although residual pores located at grain boundaries may act as local electric field concentrators, the suppression of long-range defect migration in the gradient shell structure effectively mitigates their impact on dielectric breakdown and reliability. The data points of all components in the Fig. 7(f) are in good agreement with the Weibull distribution, and the β is between 10.013 and 12.634, indicating that all the ceramics have good reliability [52]. During pre-sintering, Y preferentially occupies A-sites. Under reducing atmospheres with low oxygen partial

pressure ($pO_2 \approx 10^{-13}$ atm), Y substitution introduces donor-type defects ($Y_{Ba}^{\bullet}$), while Mg incorporation at the B-site (Mg_{Ti}'') acts as an acceptor. In this co-doped system, charge neutrality is predominantly maintained through ionic compensation between donor- and acceptor-type defects. Oxygen vacancies ($V_O^{\bullet\bullet}$) are primarily generated in association with acceptor substitution and are further stabilized through defect association, rather than serving as the dominant charge-compensating species. Oxygen vacancies preferentially associate with acceptor-type Mg_{Ti}'' defects to form stable complex defect clusters $[Mg_{Ti}''\text{-}V_O^{\bullet\bullet}]$ [45], while primarily $Y_{Ba}^{\bullet}$ influences defect redistribution and charge balance without directly clustering with oxygen vacancies [34,46,47].

$$Y_2O_3 \xrightarrow{BaO} 2Y_{Ba}^{\bullet} + 2e' + 2O_o + 1/2O_2 \quad (4)$$

$$MgO \xrightarrow{TiO_2} Mg_{Ti}'' + V_O^{\bullet\bullet} + O_O \quad (5)$$

TSDC measurements were performed to investigate defect-dipole relaxation and thermally activated charge-carrier dynamics in BT-based ceramics. As shown in Fig. 7(e-f), the depolarization current increases with temperature under different poling conditions, reflecting the progressive thermal activation of defect-related species. It should be noted that the depolarization peak intensity alone cannot be directly correlated with the concentration of oxygen vacancies, since the TSDC response is governed not only by defect population but also by defect-relaxation kinetics and carrier redistribution processes. In particular, at elevated temperatures approaching the paraelectric regime of $BaTiO_3$, thermally activated charge carriers become increasingly delocalized, weakening the electrical distinction between the core and shell regions [53,54]. Under such conditions, direct comparison of high-temperature depolarization peak intensity is insufficient to reliably evaluate the intrinsic oxygen-vacancy migration behavior. To obtain a more reliable physical interpretation, the activation energy of the depolarization process was extracted using the initial rise method [55]:

$$\ln[J(T)] \approx C - E_a/k_BT - (T/T_m)^4 \exp(E_a/k_BT_m - E_a/k_BT) \quad (6)$$

where C is a constant, k_B is the Boltzmann constant, E_a is the activation energy associated with space-charge migration, and T_m is the peak temperature. The calculated results show that the Pre-900 sample exhibits a higher average activation energy (~0.87 eV) compared to the Un-Pre sample (~0.78 eV), as summarized in Table S5. This increase in activation energy indicates that defect-related charge carriers in the Pre-900 sample require more thermal energy to be activated, implying stronger defect binding and reduced mobility. Therefore, the TSDC results demonstrate that pre-sintering treatment enhances defect confinement and suppresses long-range migration of oxygen vacancies.

To further evaluate the implications of these defect dynamics on electrical reliability, highly accelerated lifetime testing (HALT) was conducted under a constant DC bias of 1.5 kV mm^{-1} at 250 ℃ (Fig. 7(h)). Under these harsh conditions, both samples initially maintain high insulation resistance on the order of 10^9 Ω, indicating good intrinsic insulating behavior. The Pre-900 sample exhibits a higher initial insulation resistance of approximately 2.14×10^9 Ω. With prolonged exposure to high temperature and electric field, the insulation resistance of both samples gradually decreases due to defect-assisted conduction. Notably, the Un-Pre sample undergoes abrupt degradation after ~31 h, whereas the Pre-900 sample sustains stable operation until ~42 h before failure.These HALT results indicate that, despite the stronger high-temperature TSDC response, the Pre-900 sample possesses superior resistance to long-term electrical degradation. This confirms that pre-sintering enhances defect confinement and suppresses long-range oxygen-vacancy migration, thereby improving high-temperature reliability without compromising the insulating stability of the ceramics.

Oxygen-vacancy behavior was systematically examined by combining EPR, EELS and XPS analyses. As shown in Fig. 7(i), the EPR spectra of both samples exhibit a characteristic six-line hyperfine splitting associated with Mn-related centers, which partially overlaps with oxygen-vacancy–related signals. Although the absolute concentration of oxygen vacancies cannot be quantitatively extracted due to the

influence of Mn, a qualitative comparison based on the relative signal intensity remains meaningful. In this regard, the Pre-900 sample exhibits a noticeably lower vacancy-related EPR signal intensity than the Un-Pre sample, indicating a reduced population of active oxygen-vacancy–related paramagnetic centers after pre-sintering.

To further probe the spatial distribution of oxygen vacancies at the nanoscale, EELS-STEM mapping was then performed across three shell regions. By analyzing the Ti $L_{2,3}$ edge and O K edge intensities, the nonstoichiometric oxygen content was obtained [27,48,51]:

$$3-\delta = C_O / C_{Ti} = K_{O-Ti} I_O / I_{Ti} \quad (7)$$

where is δ oxygen deficiency, C_O and C_{Ti} are the concentration of oxygen and titanium, respectively. I_O and I_{Ti} are the integrated intensities of the O K and Ti $L_{2,3}$ edges, respectively, and $K_{O\text{-}Ti}$ is a calibration factor obtained from stoichiometric BT. As shown in Fig. 8, the Pre-900 sample exhibits a lower oxygen deficiency in the shell region, with only a gradual variation as a function of depth. This behavior indicates a reduced tendency for oxygen vacancies to accumulate near the grain edges, suggesting that their long-range migration is effectively hindered. In contrast, the Un-Pre sample shows a much steeper oxygen-deficiency gradient, with pronounced vacancy enrichment in the shell region, which is detrimental to electrical reliability. It should be noted that the EELS analyses presented here are based on representative shell regions examined across multiple grains. While inherently local in nature, the observed trends are reproducible and are further supported by consistent macroscopic evidence from impedance spectroscopy and highly accelerated lifetime testing (HALT), collectively indicating enhanced vacancy confinement in the Pre-900 sample.

In addition, surface-sensitive XPS analysis was employed as a supplementary, qualitative probe (Fig. S7). The O 1s spectra were deconvoluted into lattice oxygen, vacancy-related oxygen, and adsorbed oxygen components. It should be emphasized that XPS primarily reflects surface chemistry and therefore is interpreted in a comparative rather than quantitative manner. Consistent with the EPR and EELS results, the Pre-900 sample shows a reduced relative contribution of vacancy-related oxygen at

the surface compared with the Un-Pre sample. Taken together, the EPR, EELS and XPS analyses consistently indicate that pre-sintering suppresses oxygen-vacancy activity and enhances defect confinement, rather than directly reducing the total bulk oxygen-vacancy concentration [48–50].

It should also be emphasized that high-temperature TSDC primarily probes the thermally activated release of mobile defect-related charge carriers, which reflects short-range migration and depolarization processes rather than the absolute concentration of oxygen vacancies. Accordingly, the higher depolarization current observed for the Pre-900 sample at elevated temperatures indicates enhanced activation of localized defect carriers. In contrast, impedance spectroscopy, HALT measurements, and EPR analysis consistently reveal suppressed long-range oxygen-vacancy migration and improved resistance to defect-driven degradation after pre-sintering. Collectively, these results suggest that the pre-sintering process introduces a graded compositional-gradient shell structure that promotes defect localization and effectively enhances breakdown strength and high-temperature reliability in $BaTiO_3$-based MLCC dielectrics.

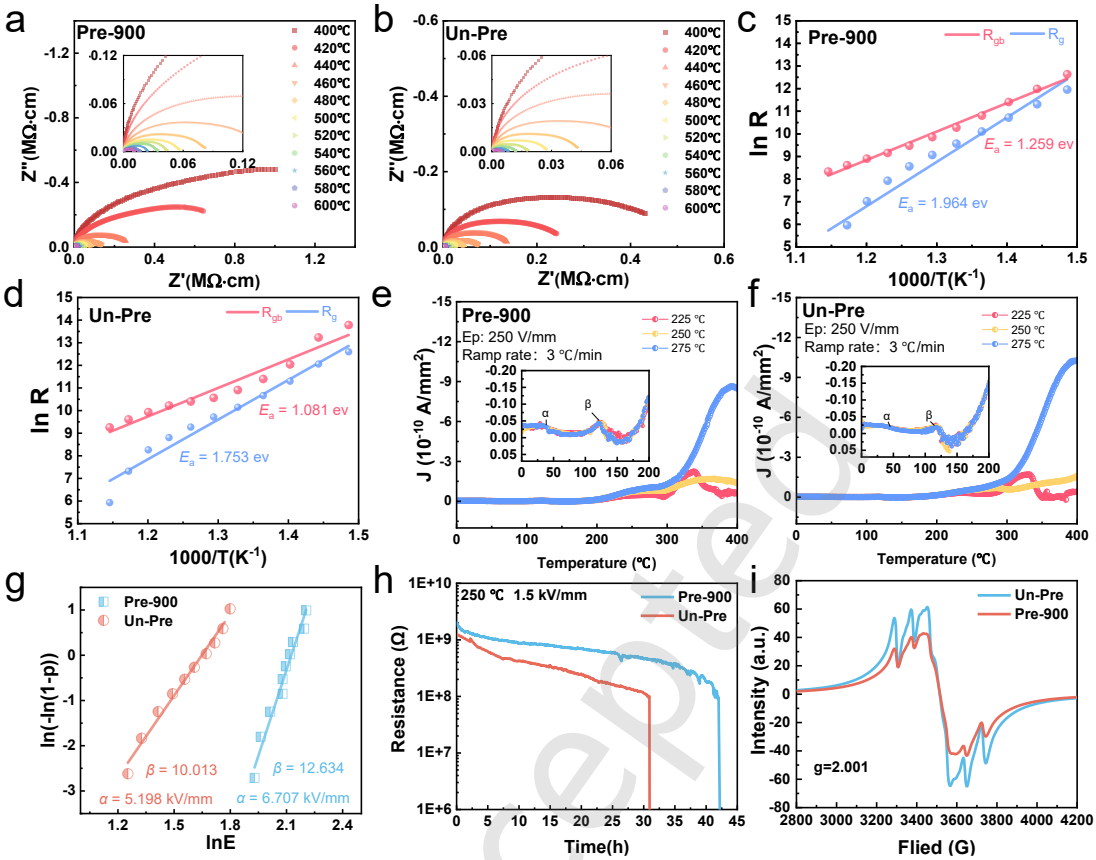

Fig. 7 (a–b) Cole-Cole impedance plots from 400–600 ℃. (c–d) Arrhenius fits for grain and grain boundary resistances. (e-f) Comparison of TSDC curves between Pre-900 and Un-pre samples. (g) Weibull distribution of breakdown strength. (h) HALT data map of the two samples. (i) The EPR spectra.

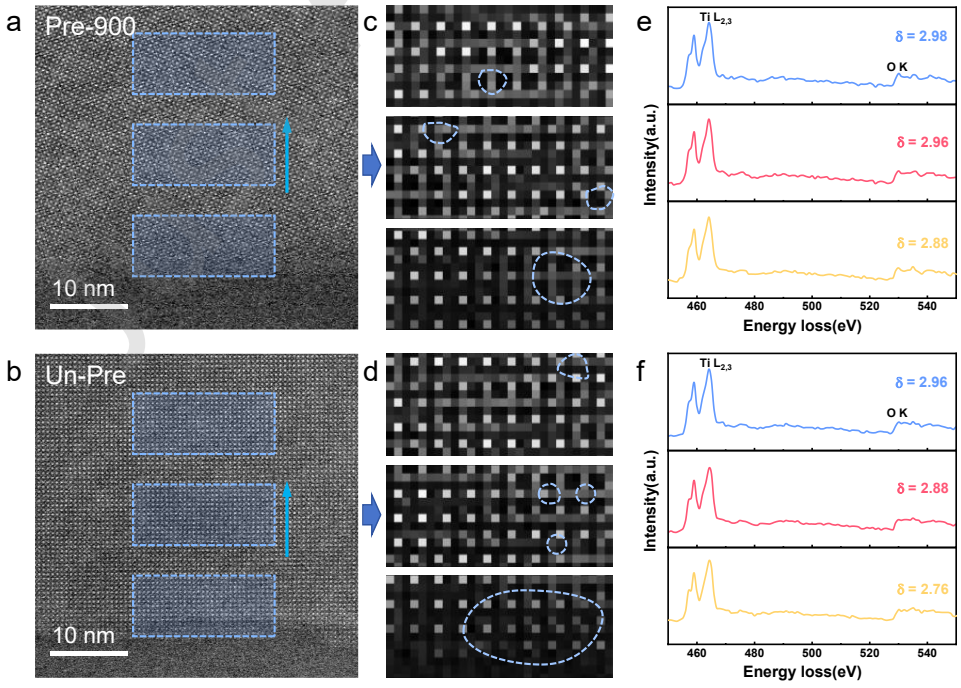

Fig. 8 (a–b) HAADF-STEM image of the near grain boundaries. (c–d) EELS scan signals across the shell region. (e–f) EELS area-scan results and corresponding oxygen-deficiency values.

4. Conclusion

This study presents a mechanistically explicit design strategy for $BaTiO_3$-based dielectrics by integrating compositional gradient design with nano-domain engineering to simultaneously enhance dielectric constant, temperature stability, and electrical reliability. A controlled pre-sintering step at 900 °C is introduced to induce a pronounced redistribution of Y/Mg/Mn dopants, resulting in a well-defined tetragonal core with a graded compositional-gradient shell microstructure. Comprehensive structural characterization confirms that Y^{3+} enrichment toward the inner part of the graded shell forms an effective defect-isolation region that suppresses further dopant diffusion, while the gradual segregation of Mg and Mn toward the outer shell promotes the formation of defect complexes that immobilize oxygen vacancies. This engineered compositional gradient significantly increases the activation energy for vacancy migration and enhances the stability of the insulating shell under high electrical and thermal stress conditions. Simultaneously, nanoscale polar regions develop at the compositionally graded core–shell interfaces, disrupting long-range ferroelectric order and giving rise to a diffuse, relaxor-like polarization behavior. The synergistic interaction between defect confinement and nanoscale domain dynamics enables a high dielectric constant (ε_r > 2200), X8R-grade thermal stability (−55–150 °C, $\Delta C/C_{25°C} \leq \pm 15\%$), and markedly improved breakdown strength (> 6.7 kV/mm). The correlations established in this work among microstructure evolution, dopant redistribution, and defect–domain interactions provide a materials-level understanding of how compositional-gradient design can be used to balance capacitance and reliability in $BaTiO_3$-based dielectrics. It should be emphasized that the present results are obtained at the bulk ceramic materials level, and further investigations will be required to bridge the gap between laboratory processing and practical MLCC fabrication, particularly in multilayer configurations and ultrathin dielectric layers. Beyond MLCC-related applications, the concepts of controlled dopant redistribution, compositional-gradient shells, and defect-mediated domain regulation may also offer a useful design guideline for the development of next-generation high-performance perovskite dielectric

ceramics.

Acknowledgments

This study was supported by the Ministry of Industry and Information Technology of China under Project High-Dielectric/Conductive Rare-Earth Ceramic Materials (CEIEC 2024-ZM02-0052), National Key Research Program of China (Grant No. 2022YFB3807403), National Science Foundation of China (Grant No. 51802142), Natural Science Foundation of Guangdong Province (Grant No. 2022A1515012604), Foundation of State Key Laboratory of New Electronic Components and Materials (Grant No. FHR-JS-202011012), and Joint Innovation Center of Advanced Electronic Components and Materials (Grant No. FHR-JS-202103001).

Competing interest

The authors declare that they have no known competing financial interests or personal relationships that could have appeared to influence the work reported in this paper.

Electronic Supplementary Material

Supplementary figures (Fig. S1–S7) and tables (Table S1–S4) are available in the online version of the article.

References

[1] Alkathy MS, Milton FP, Gatasheh MK, *et al.* Enhancing dielectric properties and thermal stability in microwave-synthesized Nd-modified barium titanate nanoceramics for possible MLCC applications. *Appl Phys A* 2024, 130: 402.

[2] Li F, Cabral MJ, Xu B, *et al*. Giant piezoelectricity of Sm-doped $Pb(Mg_{1/3}Nb_{2/3})O_3$ -$PbTiO_3$ single crystals. *Science* 2019, 364: 264–8.

[3] Dai SW, Li MY, Wu XW, *et al.* Combinatorial optimization of perovskite-based ferroelectric ceramics for energy storage applications. *J Adv Ceram* 2024, 13: 877–910.

[4] Chun JS, Kim J, Lee WW, *et al.* Effective rare-earth doping on semiconductor behavior for $BaTiO_3$-based automotive MLCCs. *Ceram Int* 2024, 50: 42963-42968.

[5] Song Y, Zhang M, Lan S, *et al.* High-temperature $BaTiO_3$-based ceramic capacitors by entropy

engineering design. *J Adv Ceram* 2024, 13(9): 1498-1504.

[6] Li W, Shen ZH, Liu RL, *et al.* Generative learning facilitated discovery of high-entropy ceramic dielectrics for capacitive energy storage. *Nat Commun* 2024, 15: 4940.

[7] Luo WJ, Yan S, Zhou J. Ceramic-based dielectric metamaterials. *Interd Mater* 2022, 1: 11–27.

[8] Hong K, Lee TH, Suh JM, *et al.* Perspectives and challenges in multilayer ceramic capacitors for next generation electronics. *J Mater Chem C* 2019, 7: 9782–9802.

[9] Yao FZ, Yuan Q, Wang Q, *et al.* Multiscale structural engineering of dielectric ceramics for energy storage applications: from bulk to thin films. *Nanoscale* 2020, 12: 17165–17184.

[10] Gigli L, Veit M, Kotiuga M, *et al*. Thermodynamics and dielectric response of $BaTiO_3$ by data-driven modeling. *Npj Comput Mater* 2022, 8: 209.

[11] Buscaglia V, Randall CA. Size and scaling effects in barium titanate. An overview. *J Eur Ceram Soc* 2020, 40: 3744–3758.

[12] Luan SW, Si SK, Zhang L, *et al.* Fabrication of $BaTiO_3$ nanopowders with high tetragonality via two-step assisted rotary furnace calcination for MLCC applications. *Ceram Int* 2023, 49: 12529–12539.

[13] Wang PF, Huang X, Luan SW, *et al.* Exceptional dielectric performance of MLCCs enabled by defect-engineered $BaTiO_3$. *J Mater Chem C* 2024, 12: 13131–13140.

[14] Zhen YC, Xiao MJ, Cheng X, *et al.* Defect control of Yb-doped dielectric ceramics on improving the reliability for MLCC application. *Ceram Int* 2023, 49: 12097–12104.

[15] Lin YZ, Yang KH, Hsiang HI. Effect of A/B ratio on the dielectric properties and insulation resistance of barium titanate sintered in a reducing atmosphere. *Mater Res Bull* 2024, 178: 112877.

[16] Zhang XT, Zhao LL, Liu LW, *et al.* Interface and defect modulation via a core–shell design in $(Na_{0.5}Bi_{0.5}TiO_3@La_2O_3)$-$(SrSn_{0.2}Ti_{0.8}O_3@La_2O_3)$-$Bi_2O_3$-$B_2O_3$-$SiO_2$ composite ceramics for wide-temperature energy storage capacitors. *Chem Eng J* 2022, 435: 135061.

[17] Xue KY, Xie JL, Wang ML, *et al.* Defect structure and dielectric properties of Mn-doped X8R $BaTiO_3$-based ceramics with high permittivity: Experiments and first-principle calculations. *Ceram Int* 2023, 49: 16514–16523.

[18] Cheng X, Zhen YC, Xiao MJ, *et al*. Diffusion and defect chemistry of temperature-stable $BaTiO_3$-based ceramics: Experiment and theoretical calculations. *J Eur Ceram Soc* 2025, 45:

116825.

[19] Luan SW, He HZ, Zhang L, *et al.* Fabrication of high performance $BaTiO_3$ films via aqueous tape casting for ultrathin MLCC applications. *Ceram Int* 2025, 51: 50374–50383.

[20] Chen KY, Yan TX, Liu J, *et al.* Origin of the ultra-wide temperature dielectric stability and dynamic behavior of nanoregions in $0.6Bi(Mg_{0.5}Ti_{0.5})O_3–0.4Ba_{0.8}Ca_{0.2}(Ti_{0.875}Zr_{0.125})O_3$. *J Mater Chem C* 2022, 10: 16407–16419.

[21] Randall CA, Yousefian P. Fundamentals and practical dielectric implications of stoichiometry and chemical design in a high-performance ferroelectric oxide: $BaTiO_3$. *J Eur Ceram Soc* 2022, 42: 1445–1473.

[22] Yang J, Ge GL, Lin JF, *et al.* One doping strategy to simultaneously lower the sintering temperature and increase the energy storage properties. *Chem Eng J* 2022, 434: 134660.

[23] Zhu CQ, Cai ZM, Xiao MJ, *et al.* Boosting effective capacitance of nanograined $BaTiO_3$-based ceramics via a precise core-shell-structure optimization strategy. *J Alloy Compd* 2024: 174037.

[24] Zhang F, Tan JH, Wang PF, *et al.* Defect dipole engineering enhanced the dielectric performance and reliability of Mn-doped $BaTiO_3$-based multilayer ceramic capacitor. *Ceram Int* 2024, 50: 38263–38273.

[25] Ma ZY, Li Y, Zhao Y, *et al.* High-performance energy-storage ferroelectric multilayer ceramic capacitors *via* nano-micro engineering. *J Mater Chem A* 2023, 11: 7184–7192.

[26] Kim H, Ju SU, Cho J, *et al.* Fe_2O_3-assisted $(1–x)(K, Na)NbO_3–xSrZrO_3$ ceramics for X8R multilayer ceramic capacitors. *Chem Eng J* 2025, 519: 164718.

[27] Huang X, Wang PF, Zhang L, *et al.* Enhanced reliability of ultra-thin multilayer ceramic capacitors (MLCCs) based on re-oxidation process. *J Mater Sci-Mater El* 2023, 34: 1463.

[28] Lv YT, Wang PF, Qin YX, *et al.* Significantly enhanced reliability in defect-engineered $BaTi_{1-x}Mg_xO_3$ ceramics. *Ceram Int* 2024, 50: 37002–37009.

[29] Izawa K, Utsunomiya M, Inayama S, *et al.* Visualization of resistance distribution and microstructure in locally degraded multilayered ceramic capacitor. *Appl Phys Lett* 2023, 123: 142902.

[30] Chen K, Zhao P, Chen JJ, *et al.* Broad temperature span and large electrocaloric effect in lead-free ceramics via multi-strategy synergistic optimization. *Chem Eng J* 2024, 502: 157863.

[31] Jeon SC, Yoon BK, Kim KH, *et al.* Effects of core/shell volumetric ratio on the dielectric-

temperature behavior of $BaTiO_3$. *J Adv Ceram* 2014, 3: 76–82.

[32] Zhang M, Lan S, Yang BB, *et al*. Ultrahigh energy storage in high-entropy ceramic capacitors with polymorphic relaxor phase. *Science* 2024, 384: 185–9.

[33] Hwang TY, Choi Y, Song Y, *et al.* Correlation between tetragonality (c/a) and direct current (dc) bias characteristics of $BaTiO_3$-based multi-layer ceramic capacitors (MLCC). *J Mater Chem C* 2018, 6: 972–979.

[34] Wang XF, Fan YX, Luo GQ, *et al.* Effect of yttrium (Y) substitution on the structure and dielectric properties of $BaTiO_3$. *Ceram Int* 2023, 49: 9042–9051.

[35] Wei JW, Shang F, Zhang HB, *et al.* Improving the energy storage performance of $BaTiO_3$-based glass ceramics by reconstituting glass network structure via electronegativity tuning. *J Materiomics* 2025, 11: 100873.

[36] Meng YZ, Liu K, Zhang XY, *et al.* Defect engineering in rare-earth-doped $BaTiO_3$ ceramics: Route to high-temperature stability of colossal permittivity. *J Am Ceram Soc* 2022, 105: 5725–5737.

[37] Tang T, Liu D, Wang L, *et al.* Ultrahigh energy storage density and efficiency of antiferroelectric $AgNbO_3$-based MLCCs via reducing the off-center cations displacement. *Chem Eng J* 2025, 503: 158557.

[38] Park S, Kim S, Lee C, *et al.* A-/B-site engineering of $AgNbO_3$-based ceramics for high-efficiency relaxor antiferroelectric energy storage. *J Adv Ceram* 2025, 14: 9221174.

[39] Wang J, Gao RZ, Tang SY, *et al*. General principle of ferroelectric topological domain formation. *Sci Adv* 2025, 11: eadu6223.

[40] Zhang WC, Jiang Y, Xiao MJ, *et al.* High DC-Bias Stability and Reliability in $BaTiO_3$ -Based Multilayer Ceramic Capacitors: The Role of the Core–Shell Structure and the Electrode. *Acs Appl Mater Inter* 2023: 16(1): 1158-1169.

[41] Hsiang HI, Yang YH, Huang CY, *et al.* Effects of calcination on the dielectric properties and insulation resistance of $Ba_{0.95}Ca_{0.05}TiO_3$ ceramics sintered in a reducing atmosphere. *J Alloy Compd* 2023, 960: 170919.

[42] Liu JK, Ding YQ, Li CY, *et al*. Relaxor ferroelectric $(Bi_{0.5}Na_{0.5})TiO_3$-based ceramic with remarkable comprehensive energy storage performance under low electric field for capacitor applications. *J Mater Sci Mater Electron* 2021, 32: 21164–21177.

[43] Luo ZX, Lan S, Yang BB, *et al*. Entropy-assisted low-electrical-conductivity pyrochlore for capacitive energy storage. *Acta Materialia* 2024, 275: 120079.

[44] Li Y, Wu J, Zhang ZG, *et al.* Improving the electric energy storage performance of multilayer ceramic capacitors by refining grains through a two-step sintering process. *Chem Eng J* 2024, 479: 147844.

[45] Huang JY, Chen R, Xing JJ, *et al.* Core–rim structure evolution and electric properties of Ca–Mg–Dy-co-doped $BaTiO_3$ ceramics. *J Mater Chem C* 2023, 11: 4784–4791.

[46] Park JH, Kim ES. Effects of MgO and Rare-Earth Oxides (Y_2O_3, Yb_2O_3, Dy_2O_3) on the Structural Characteristics and Electrical Properties of $BaTiO_3$. *Processes* 2023, 11: 3235.

[47] Gu Y, Zhang FQ, Wu WW, *et al.* Microstructure regulation and failure mechanism study of $BaTiO_3$-based dielectrics for MLCC application. *J Adv Dielectr* 2023, 13: 2350002.

[48] Wang Z, Meng XY, Guo QH, *et al.* Formation and evolution of oxygen vacancy layer in $BaTiO_3$ dielectric ceramics under thermal and electric field stimuli. *Acta Mater* 2025, 299: 121450.

[49] Fan JT, He G, Long Z, *et al.* High insulation resistivity and low dielectric loss in (Ta, Al)-codoped $BaTiO_3$ colossal permittivity materials. *J Am Ceram Soc* 2024, 107: 4854–4863.

[50] Mo SY, Tang C, Zhang H, *et al.* Colossal permittivity and excellent temperature stability of $BaTiO_3$ based fine ceramics with controlled grain growth. *Ceram Int* 2024, 50: 11980–11988.

[51] Kaneda K, Lee S, Donnelly NJ, *et al.* Kinetics of Oxygen Diffusion into Multilayer Ceramic Capacitors During the Re-oxidation Process and its Implications on Dielectric Properties. *J Am Ceram Soc* 2011, 94: 3934–3940.

[52] Yang H, Tian J, Lin Y, et al. Realizing ultra-high energy storage density of lead-free $0.76Bi_{0.5}Na_{0.5}TiO_3$-$0.24SrTiO_3$-$Bi(Ni_{2/3}Nb_{1/3})O_3$ ceramics under low electric fields. *Chem Eng J* 2021, 418: 129337.

[53] Hsu H J, Yang K H, Hsiang H I. Enhanced dielectric properties and thermal stability of $BaTiO_3$ ceramics sintered in a reducing atmosphere through $MnNb_2O_6$ doping. *Ceram Int* 2025, 51(15): 19910-19922.

[54] Yousefian P, Akkopru-Akgun B, Randall C A, et al. Electrical degradation in dielectric and piezoelectric oxides: Review of defect chemistry and characterization methods. *Prog Mater Sci* 2025, 153: 101473.

[55] Akkopru-Akgun B, Marincel D M, Tsuji K, et al. Thermally stimulated depolarization current

measurements on degraded lead zirconate titanate films. *J Am Ceram Soc* 2021, 104(10): 5270-5280.